A Multicomponent Magnetic Proxy for Solar Activity

Harry P. Warren[1], Linton E. Floyd[2], and Lisa A. Upton[2]

[1]Space Science Division, Naval Research Laboratory, Washington, DC 20375 USA
[2]Space Systems Research Corporation, Alexandria, VA, 22314, USA

Key Points:

- A new magnetic proxy for solar activity is presented
- The new magnetic proxy is well correlated with existing proxies

Corresponding author: Harry Warren, harry.warren@nrl.navy.mil

Abstract

We present a new, multicomponent magnetic proxy for solar activity derived from full disk magnetograms that can be used in the specification and forecasting of the Sun's radiative output. To compute this proxy we project Carrington maps, such as the synchronic Carrington maps computed with the Advective Flux Transport (AFT) surface flux transport model, to heliographic cartesian coordinates and determine the total unsigned flux as a function of absolute magnetic flux density. Performing this calculation for each day produces an array of time series, one for each flux density interval. Since many of these time series are strongly correlated, we use principal component analysis to reduce them to a smaller number of uncorrelated time series. We show that the first few principal components accurately reproduce widely used proxies for solar activity, such the the 10.7 cm radio flux and the Mg core-to-wing ratio. This suggests that these magnetic time series can be used as a proxy for irradiance variability for emission formed over a wide range of temperatures.

Plain Language Summary

Proxies for solar activity are often used to extend solar irradiance measurements in time or forecast future variability. Widely used proxies, such as the 10.7 cm radio flux, can include emission formed from different mechanisms, which limits their ability to accurately reproduce some irradiance time series. Other proxies, such as the Mg core-to-wing ratio, perform better, but are taken from different space instruments, whose long-term calibration can be difficult to understand. In this paper we show how to use images of the solar photospheric magnetic field to create a multicomponent proxy for solar activity that overcomes some of the limitations of existing proxies.

1 Introduction

Information on the solar spectral irradiance and its variability is needed to understand the state of the Earth's upper atmosphere. Ideally, the spectral irradiance at all wavelengths would be monitored continuously. Since this must be done from space, most spectral irradiance measurements are available for only for limited intervals of time. To extrapolate irradiance measurements to other times, proxies for solar activity are used in a regression model. Furthermore, forecasts of solar activity focus on forecasting the proxies rather than forecasting the spectral irradiance directly. Thus proxies for solar activity play an important role in understanding the near-Earth environment.

The 10.7 cm radio flux (F10, Tapping (2013)) is a widely used proxy for solar activity. This ground-based radio measurement has been made almost daily since the late 1940's and appears to be very stable. A long time series of radio measurements at several frequencies is also available from the Nobeyama Radio Observatory (Tanaka et al., 1973). Comparisons of F10 and irradiance time series, however, often show a nonlinear dependance and regression models often use F10 and its 81-day running mean as independent variables in a multiple linear regression to improve the correlation (Lean et al., 2009). The Mg core-to-wing ratio (Heath & Schlesinger, 1986), which uses the properties of the Mg II h and k doublet near 280 nm, is another widely used proxy. This emission must be observed from space and the extended core-to-wing time series stitches together measurements from a number of different instruments, each of which has different capabilities.

It has long been recognized that the Sun's radiative output is strongly correlated with the magnetic field (Gurman et al., 1974), which has been measured extensively over the past 50 years using both ground based and space based instruments. Furthermore, almost all of these measurements are spatially resolved, yielding information

on the distribution of magnetic flux on the solar surface. Finally, the evolution of the surface magnetic field is well described by models, which provide a physics-based framework for forecasting solar activity. Surprisingly, there are only a few studies which investigate the use of the magnetic field as a proxy for solar activity (e.g., Henney et al. (2012, 2015)).

In this paper we develop a new, multicomponent magnetic proxy for use in the specification and forecasting of the Sun's radiative output. As we will see, the multicomponent nature of this proxy is important for accurately modeling emission formed at many different temperatures in the solar atmosphere, something that is difficult with proxies such as F10. This work is primarily based on synchronic Carrington maps computed with the Advective Flux Transport (AFT) model (Upton & Hathaway, 2014b, 2014a, 2018), which assimilates observations from Michelson Doppler Imager (MDI) and The Helioseismic and Magnetic Imager Investigation (HMI) instruments (Scherrer et al., 1995, 2012). Using the magnetic field determined from a surface flux transport model makes is easy to use the proxy for forecasting and also addresses some of the limitations of magnetic field measurements made near the solar limb.

2 Magnetic Flux Histograms and Time Series

The AFT model describes how the radial component of the magnetic field on the solar surface is advected by supergranular diffusion, differential rotation, and meridional flow. The unique aspect of the model is its use of a time-dependent velocity pattern (Hathaway et al., 2010) in place of an ad hoc diffusion term to account for the transport of magnetic flux by supergranular motions. For this work we use AFT runs that are updated periodically with an observed line-of-sight magnetogram. The assimilated data is weighted to emphasize observations near disk center, so the AFT maps are dominated by the actual measurements in the region facing the Earth.

The observed magnetograms are taken from the Michelson Doppler Imager (MDI) on the Solar and Heliospheric Observatory (SoHO), which operated from 1996 to 2011, and the Helioseismic and Magnetic Imager (HMI, Scherrer et al. (2012)) on the Solar Dynamics Observatory (SDO), which began operations in 2010. For the HMI data, hourly synoptic data is assimilated. For MDI the synoptic data is available every 96 minutes. The magnetic field measurements from the two instruments have some subtle differences (Liu et al., 2012), which are accounted for before the data is assimilated. Because of the extended loss of contact with SoHO in 1998, we begin our analysis on April 1, 1999, transition to using AFT maps based on HMI on June 1, 2010, and end our analysis on December 31, 2020. We computed a total 7947 AFT magnetograms during this time, one for each day. The AFT calculation takes about one day of actual time for each year of the simulation.

An example Carrington map from AFT is shown in Figure 1. Here we also show a projection of the Carrington map to heliographic cartesian coordinates and a corresponding observed HMI magnetogram. Because the model is updated regularly, the Earth-facing side of the Sun heavily weighted by the data and the images are very similar. The primary advantage of using the AFT model instead of the observed magnetic flux is that the field at the limb is less noisy and does not suffer from "canopy" effects, where strong flux at the limb has the wrong sign because of projection effects. One limitation of the model is that flux that has emerged on the far side and has just rotated over the limb is not fully assimilated immediately. Both of these effects, though subtle, are evident in this example.

Anticipating comparisons with F10, which is measured between 17 and 23 UT, we compute the magnetogram images for 16 UT, the closest time for which AFT snapshots are available. Perhaps the simplest approach to constructing a proxy for solar activity

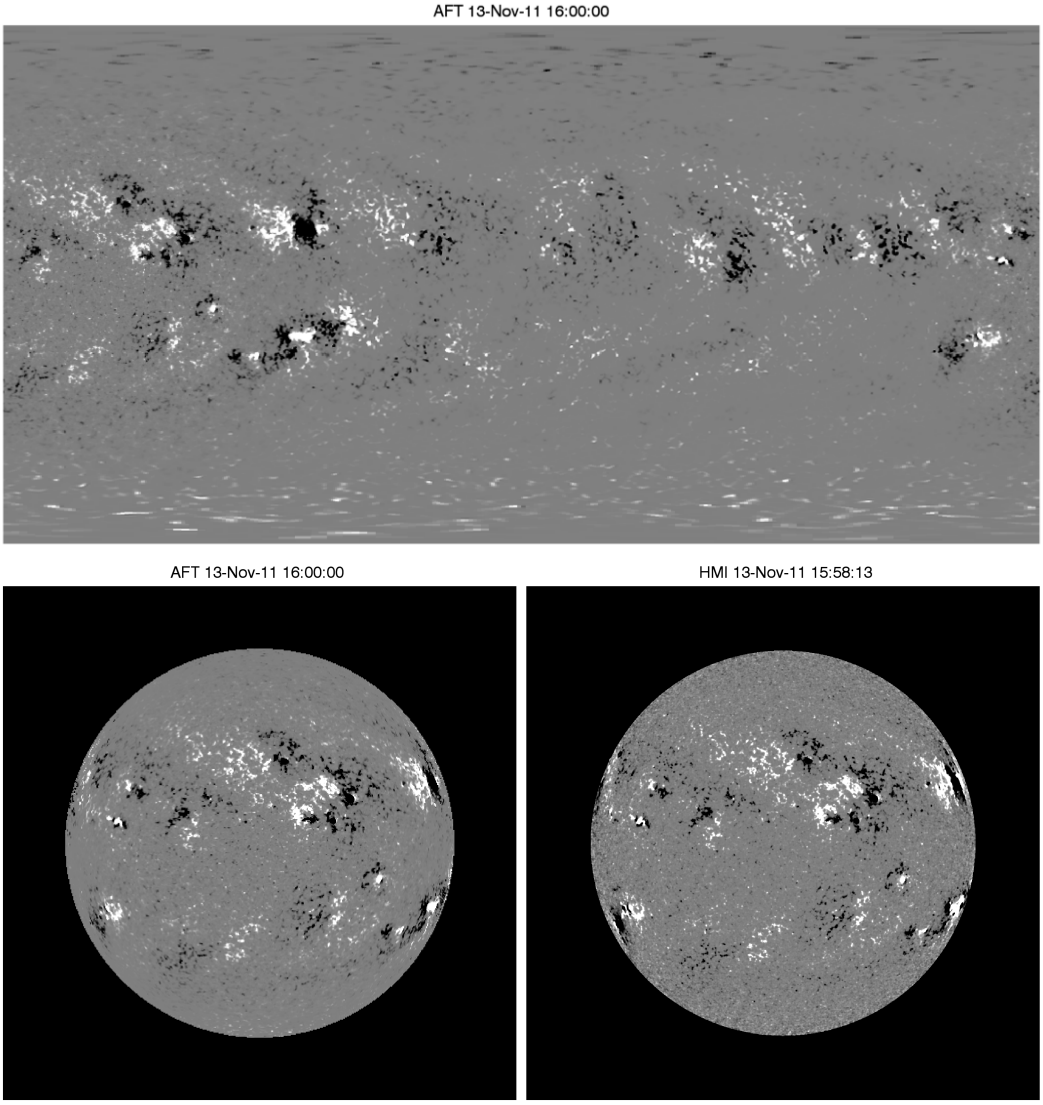

Figure 1. (top panel) An example snapshot from the AFT calculation of the surface magnetic flux. (bottom left) The AFT Carrington map projected to heliographic cartesian coordinates. (bottom right) An HMI magnetogram from approximately the same time. The magnetogram has been smoothed to the spatial resolution of the AFT image and corrected to account for the line-of-sight projection. The AFT and HMI images are generally very similar, but there are some differences at the limb. Because of project effects, strong flux at the west limb has the wrong sign. Newly emerged flux at the east limb has not been fully assimilated into the model.

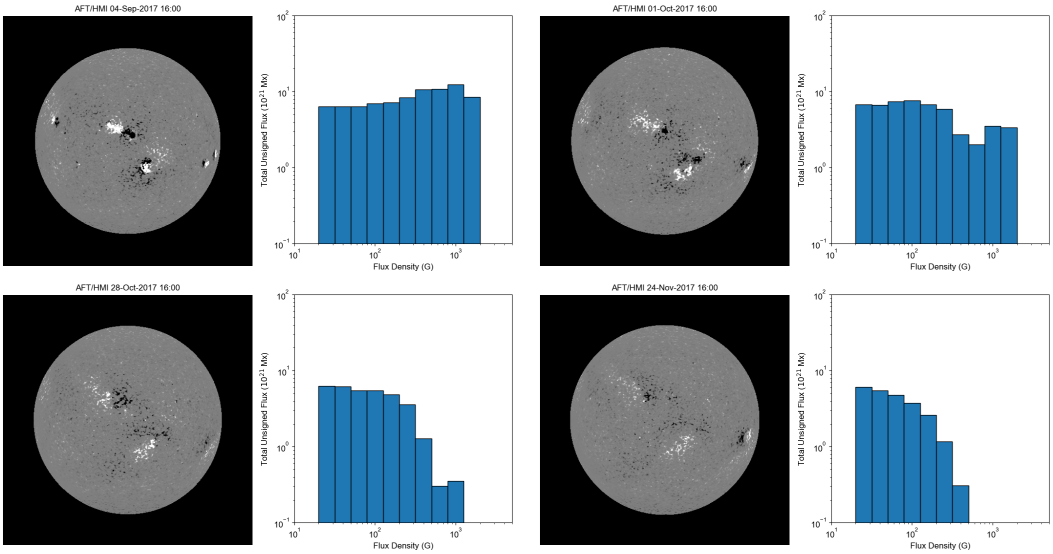

Figure 2. Example histograms of total unsigned magnetic flux as a function of magnetic flux density for four days in 2017. The magnetograms were computed from the AFT maps. The strong temporal variability of the largest fluxes is evident.

from these images would be to compute the total unsigned flux for each image, that is, the sum of the absolute magnitude of the flux density in each pixel multiplied by the pixel area. The relationship between the radiance and the magnetic field, however, can be complex. The strong magnetic fluxes found in sunspots, for example, rarely produce bright emission (e.g., Tiwari et al., 2017). Similarly, the weakest quiet sun fluxes are always present and unlikely to be strongly correlated with variations in the irradiance. One might imagine defining different ranges of fluxes to represent different components of variability (e.g., quiet Sun, active network, active region), but it is not clear how to define these boundaries.

For this work we adopt a two step procedure that circumvents these problems. We first construct histograms of the unsigned magnetic flux as a function of flux density for each day. We then perform principal component analysis (PCA) on the resulting time series to reduce them to a more manageable size. Recall that PCA is a technique for reducing the dimensionality of a dataset by defining a new orthonormal basis that is ordered by information content. Typically, the first few components account for a large percentage of the variance in the data.

Figure 2 illustrates the calculation of histograms for four days, each approximately one solar rotation apart, in late 2017 when several large active regions emerged on the disk and decayed over time. Here 10 logarithmically spaced bins between 20 and 2000 G have been chosen to compute these distributions. The lower value does not include 0 because very weak fluxes are difficult to measure. The noise level in the magnetograms is estimated to be about 10 G (Yeo et al., 2014), and is likely to be higher near the limb.

Time series for selected bins are shown in Figure 3. These time series of total unsigned flux show modulation over both rotational and solar cycle time scales. The amplitude of this modulation increases with increasing magnetic flux density. As one would expect, the fluxes in adjacent bins are strongly correlated, indicating that some of the information in these time series is redundant.

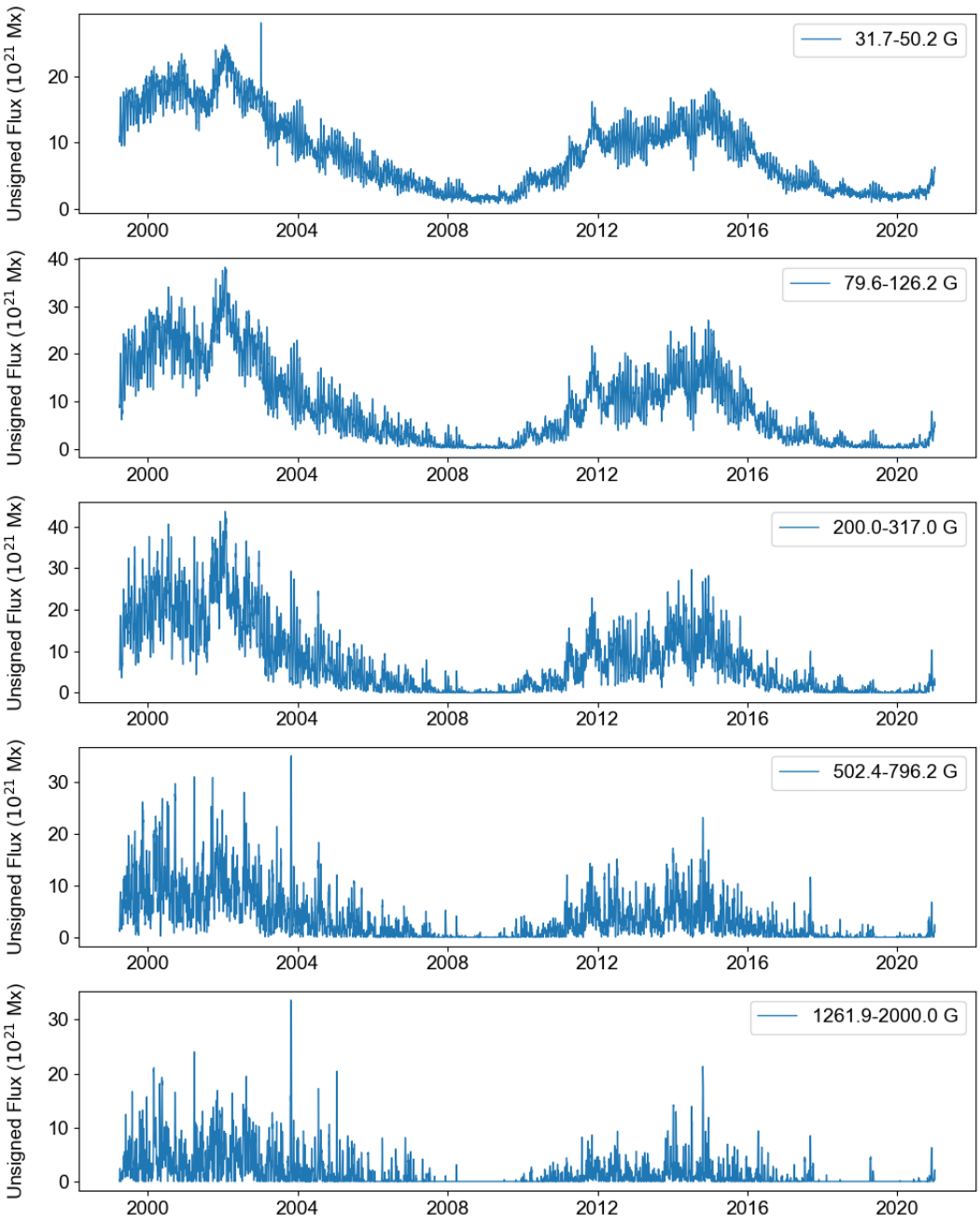

Figure 3. Time series of the total unsigned magnetic flux (flux density times pixel area in units of 10^{21} Mx) for selected flux density bins bins.

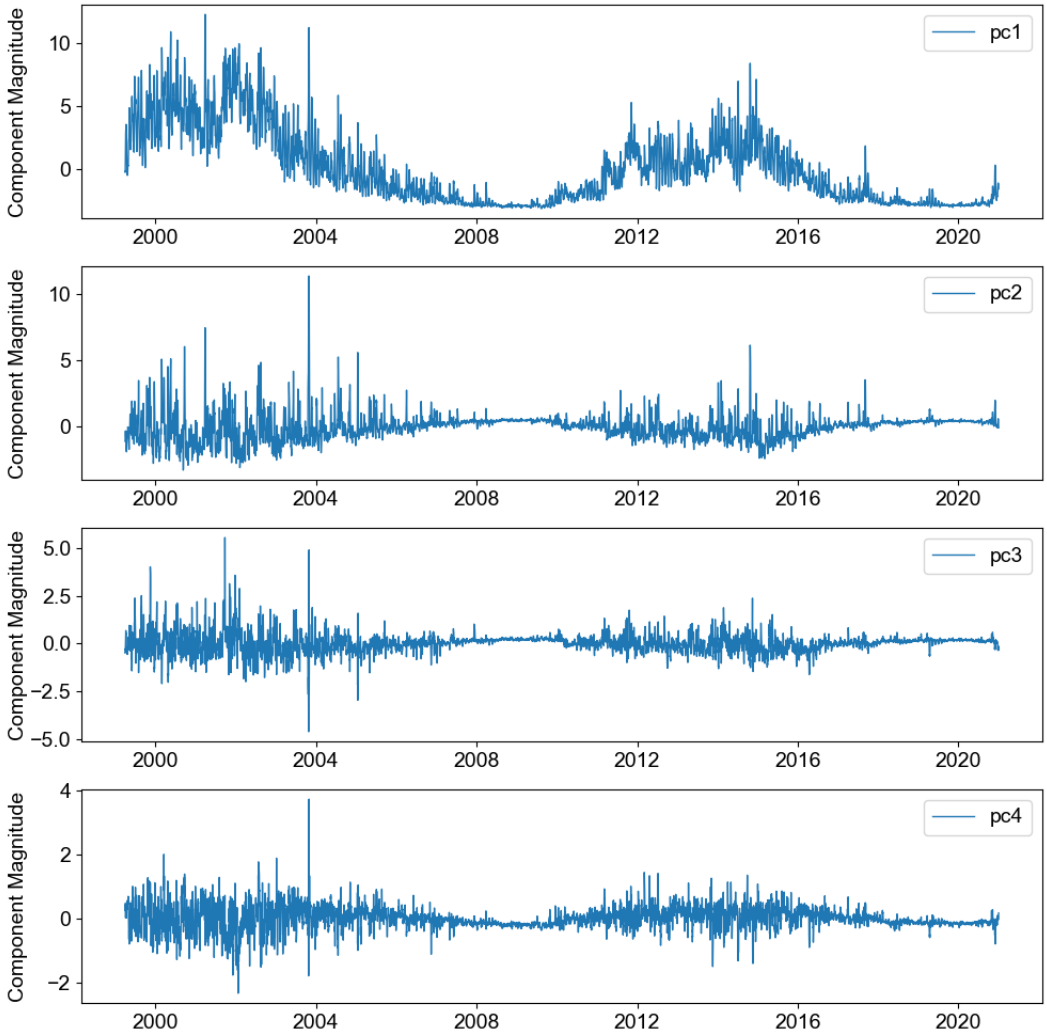

Figure 4. Time series of the first four principal components. Together, these components account for 99% of the variance in the original time series. Note that each time series has been normalized so that the components are dimensionless.

We use the PCA package from scikit-learn (Pedregosa et al., 2011) to compute the principle components of the magnetic time series. The first four components, which account for 85, 95, 98, and 99% of the variance in the original time series of magnetic fluxes, are shown in Figure 4. Note the the magnetic time series are scaled to have zero mean and unit variance before the PCA decomposition is computed. Thus the components are dimensionless.

3 Example Applications

The processed magnetic time series shown in Figure 4 can be used to model the temporal variability of solar irradiance time series. To illustrate this application we show that the magnetic time series can capture the evolution of F10, the Mg core-to-wing ratio, several frequencies observed at the Nobeyama Radio Observatory, and several irradiance time series from EUV Variability Experiment (EVE, Woods et al. (2012)) on *SDO*. For all of these time series we will perform a simple multiple linear regression of the form

$$\text{Irradiance}(t) = c_0 + \sum_{i=1}^{4} c_i M_i(t), \tag{1}$$

where $M_i(t)$ is a PCA component of the magnetic time series. We use use the Python `statsmodel` package (Seabold & Perktold, 2010) to perform these fits. The sources of these data are described in Section 5.

3.1 F10

We fit all of the available magnetic data and F10 to Equation 1. In Figure 5 we show a time series of the observed F10 and the values inferred from the fit. Also shown are the a correlation between the modeled and observed values, the residuals as a function of time, and a histogram of the residuals. To highlight the variation of the irradiance over a solar rotation, time series for smaller time ranges are also shown in Figure 5.

The model fits the observations of F10 very well. The correlation between the modeled and observed values is 0.98. The residuals are relatively small, with a standard deviation of 6.4%. The residuals are generally biased towards larger values, where the model systematically under-predicts the observations. Some of these differences may be due to very large sunspots that influence the F10 measurements, but are not well captured by the magnetograms (e.g., September 2017). Flares could also influence the F10 measurements more than the magnetograms. Close inspection of the residuals suggests an unexpected secular trend between 2004 and 2015, which seems to resume around 2016. As we will see, this pattern is evident in some of the other irradiance time series. We will discuss this in some detail in Section 4.

We fit F10 using progressively more principle components to test the impact of increasing model complexity on goodness of fit. As noted earlier, The first four components account for 85, 95, 98, and 99% of the variance in the original time series. Using only the first component yields a correlation of 0.97 and a dispersion in the residuals of 7.2%. Adding the remaining components yields correlations of 0.97, 0.98, and 0.98. For the dispersion the results are 7.1%, 6.8%, and 6.4%. Thus, the first two components account for the the vast majority of the variation in the observed irradiance time series.

3.2 Mg Core-to-Wing

The fit of the Mg core-to-wing ratio to the magnetic time series is shown in Figure 6. The format of the figures is identical to Figure 5. The magnetic model,

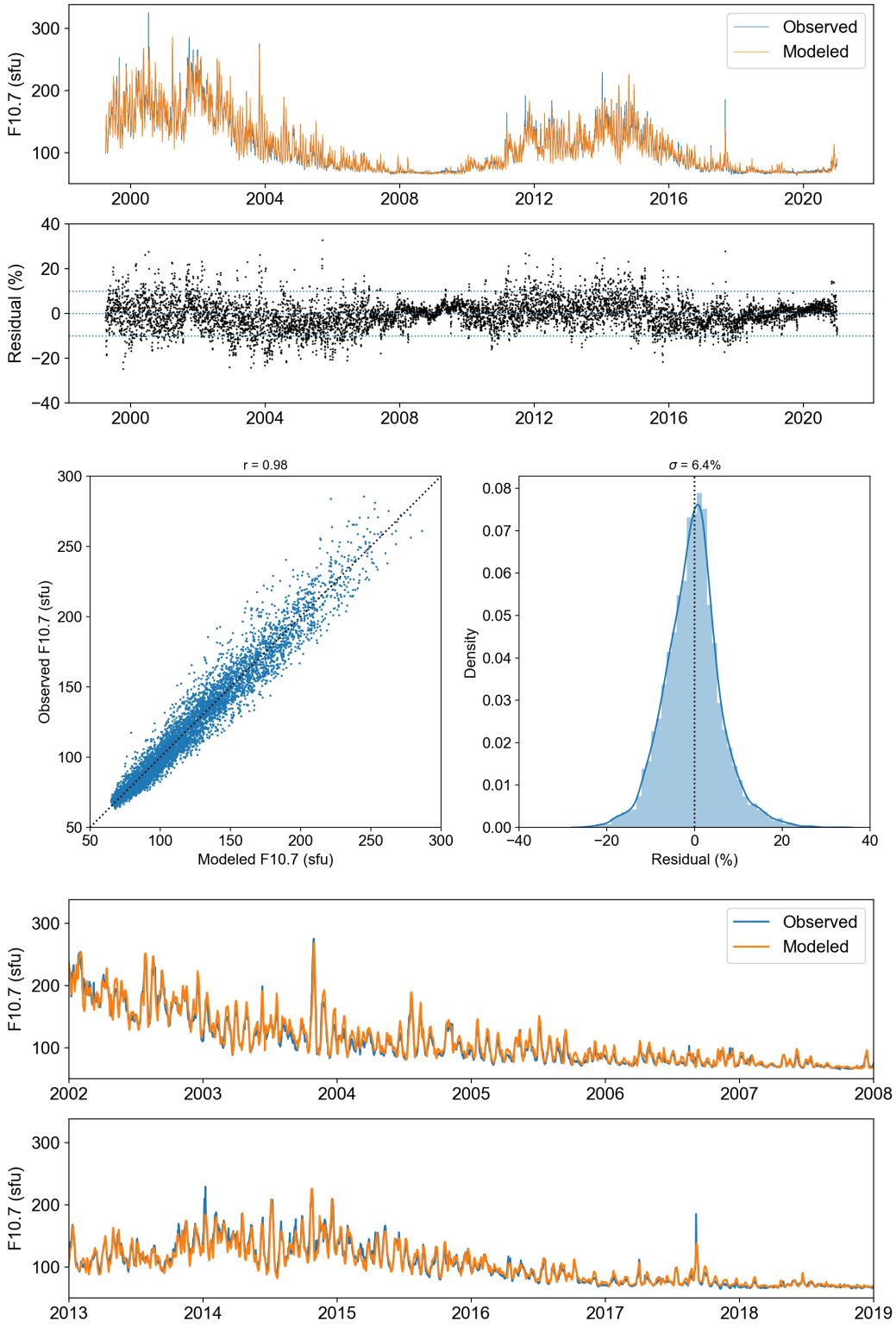

Figure 5. Results from a multiple linear regression of the magnetic flux proxy to F10. The top panels show the observed and modeled values and the residuals. The middle panels show a scatter plot of the observed and modeled value and the distribution of the residuals. The bottom panels show the observed and modeled time series over limited intervals. The model reproduces the observed values very well.

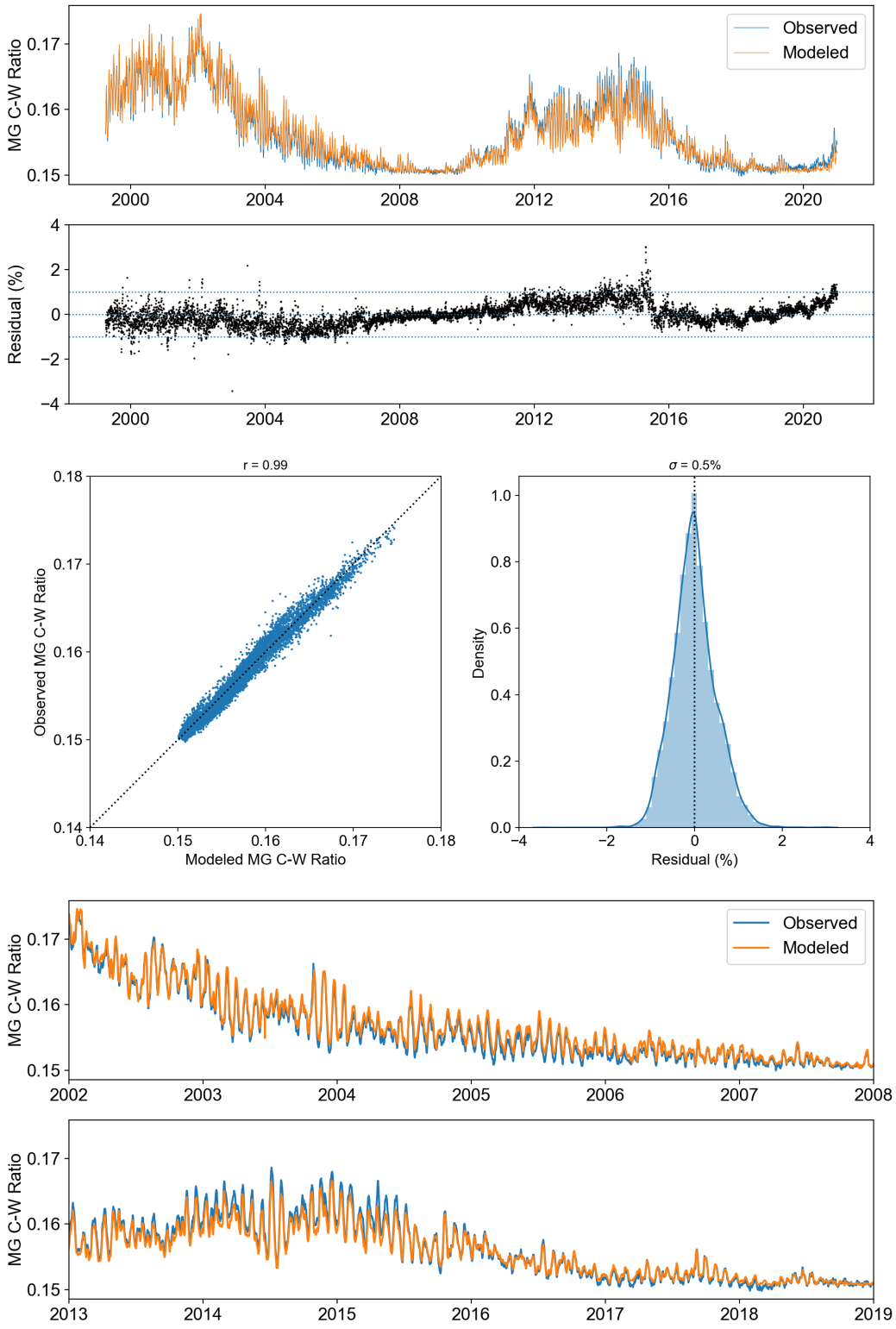

Figure 6. Results from a multiple linear regression of the magnetic flux proxy to the Mg core-to-wing ratio. The format is identical to Figure 5

Table 1. Fitting Metrics for EVE Irradiance Time Series

	Residual (%)			Correlation		
	304	195	360	304	195	360
F10	3.5	11.8	28.8	0.91	0.85	0.96
Mg	2.3	8.3	31.3	0.96	0.82	0.97
B_{PCA}	2.5	7.8	29.4	0.96	0.93	0.97

however, fits Mg better than F10. The correlation is higher and the residuals are smaller. The residuals shown in Figure 6 show the secular trends that were alluded to in the discussion on the fits to F10. Again, we will discuss possible explanation for this in Section 4.

3.3 Nobeyama Radio Observatory

Measurements of the Sun's radio emission at several frequencies have been monitored at the Toyokawa and Nobeyama radio polarimeters since the 1950's (Tanaka et al., 1973), creating long time series that are useful for irradiance modeling. Observations at 30, 15, 8, and 3.2 cm are available. Dudok de Wit et al. (2014) show that the 30 cm flux is better for modeling the thermosphere-ionosphere system. The fit of the 30 cm (1.0 GHz) signal to the magnetic time series is shown in Figure 7. The correlation and residuals are similar to those seen in the fit to F10. Here the correlation between the model and the observation is 0.98 and the dispersion in the residuals is 7.3%.

3.4 EVE

As a final application we consider fits of irradiance time series observed with EVE to the magnetic proxy. We have chosen lines formed at three different temperatures in the solar atmosphere: He II 304 Å, Fe XII 195 Å, and Fe XVI 360 Å. The first two lines were observed with the short wavelength range of EVE ("MEGS-A"), which ceased operations in May of 2014.

The observed and modeled time series, scatter plots, and histograms are shown in Figures 8, 9, and 10. The fit to He II 304 Å is very good, with small residuals over the entire time period, similar to the results from the Mg core-to-wing ratio. The fits to the other wavelengths are not as good. Fe XII 195 Å shows some relatively large discrepancies early in the EVE mission, where the model is systematically lower than the observations. The residuals are about a factor of 3 higher than those for He II 304 Å and have a large tail to negative values. The residuals for Fe XVI 360 Å are larger still, reaching values of ±100%. This is somewhat misleading, however. Fe XVI is formed at a high temperature and the signal in this line becomes very weak during solar minimum. Figure 10 shows a clear trend towards lower residuals during periods of higher solar activity. Still, even if we restrict the calculation to the core of the distribution, the residuals are about 10 times higher than they are for He II 304 Å. All of these irradiance time series show a linear relationship between the observed and modeled fluxes.

These fits of the magnetic proxy to the EVE irradiance time series can be compared with the more traditional fits to F10 or the Mg core-to-wing ratio. This is shown in Figure 11, where scatter plots of modeled and observed irradiances are displayed. The residuals from these fits show that the magnetic flux proxy performs as well as the Mg core-to-wing ratio and better than F10.

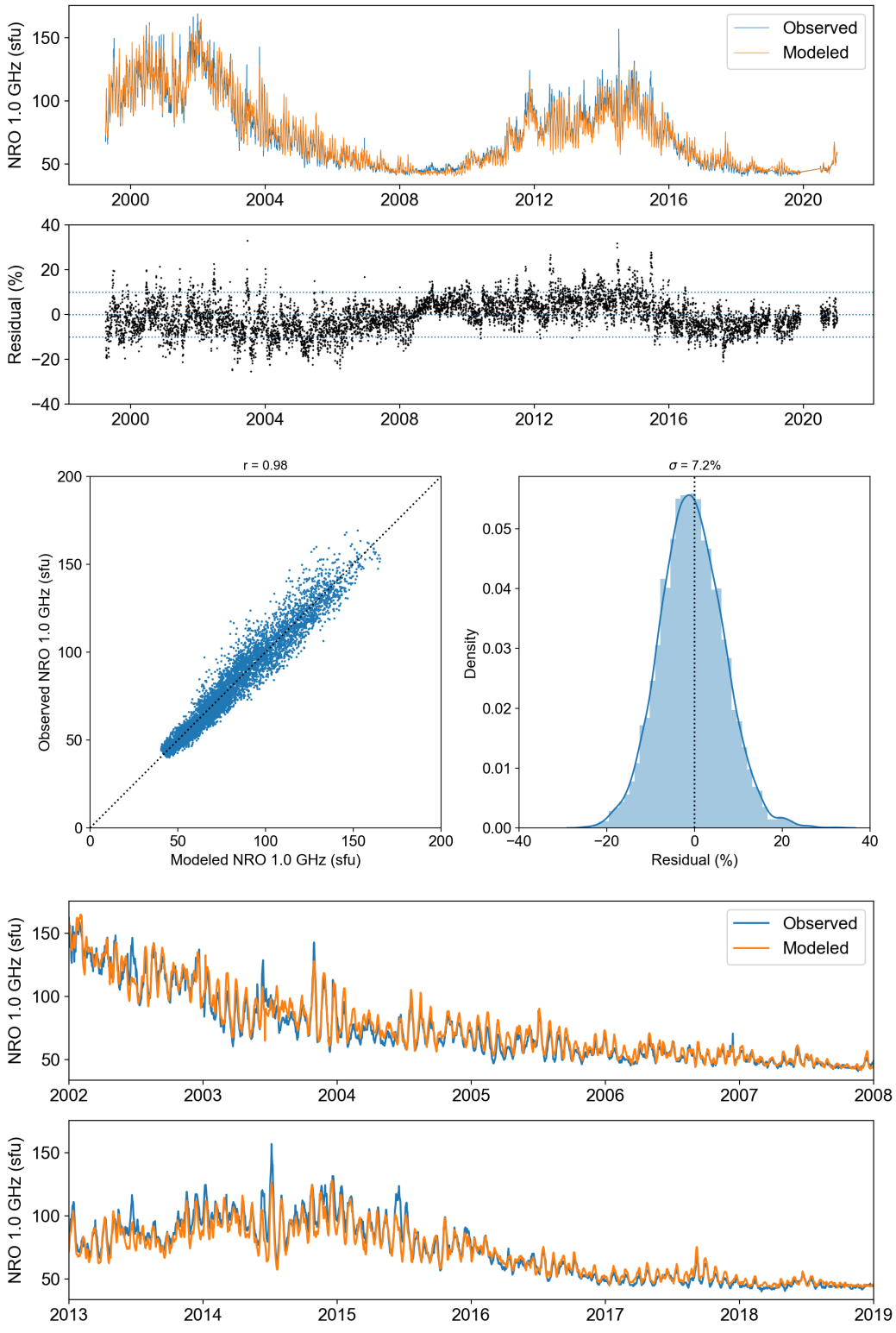

Figure 7. Results from a multiple linear regression of the magnetic flux proxy to the 1 GHz signal measured by the Nobeyama Radio Observatory. The format is identical to Figure 5.

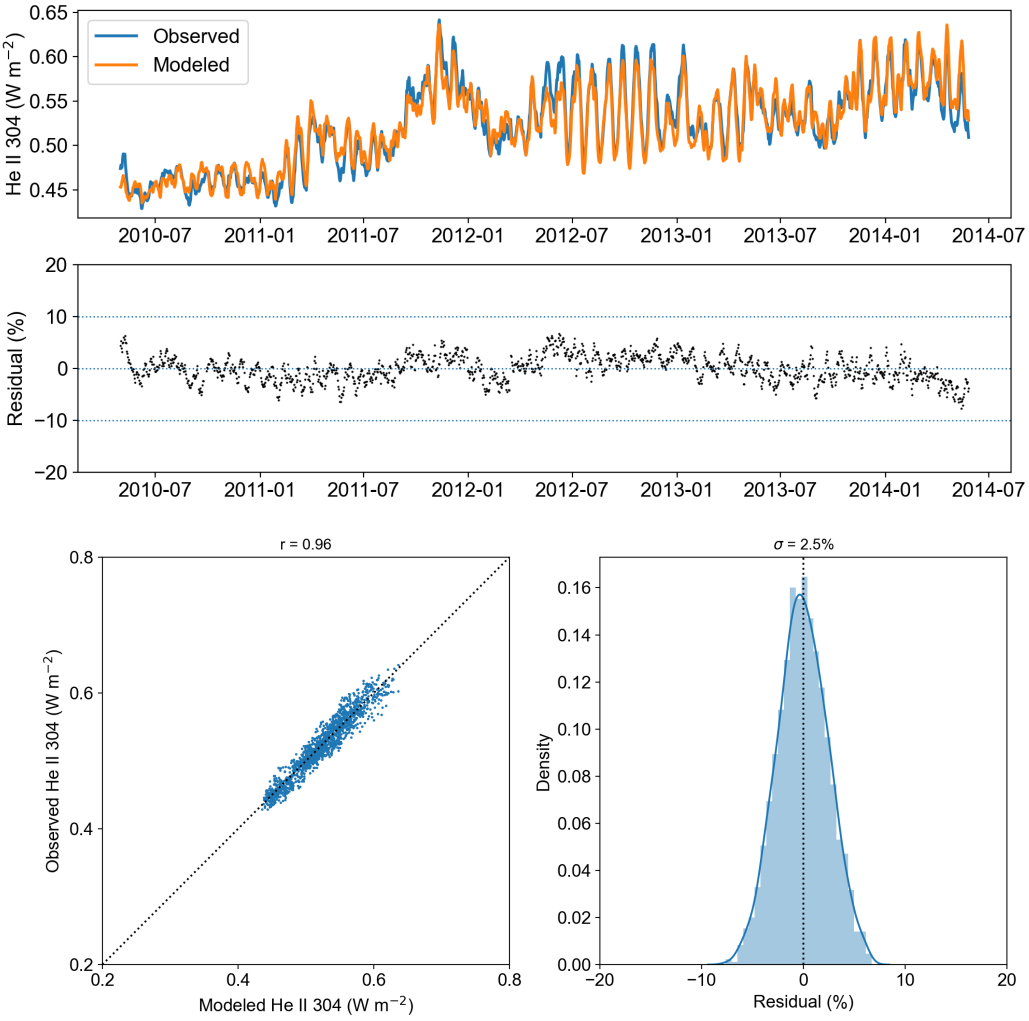

Figure 8. Results from a multiple linear regression of the magnetic flux proxy to the He II 304 Å irradiance observed with EVE.

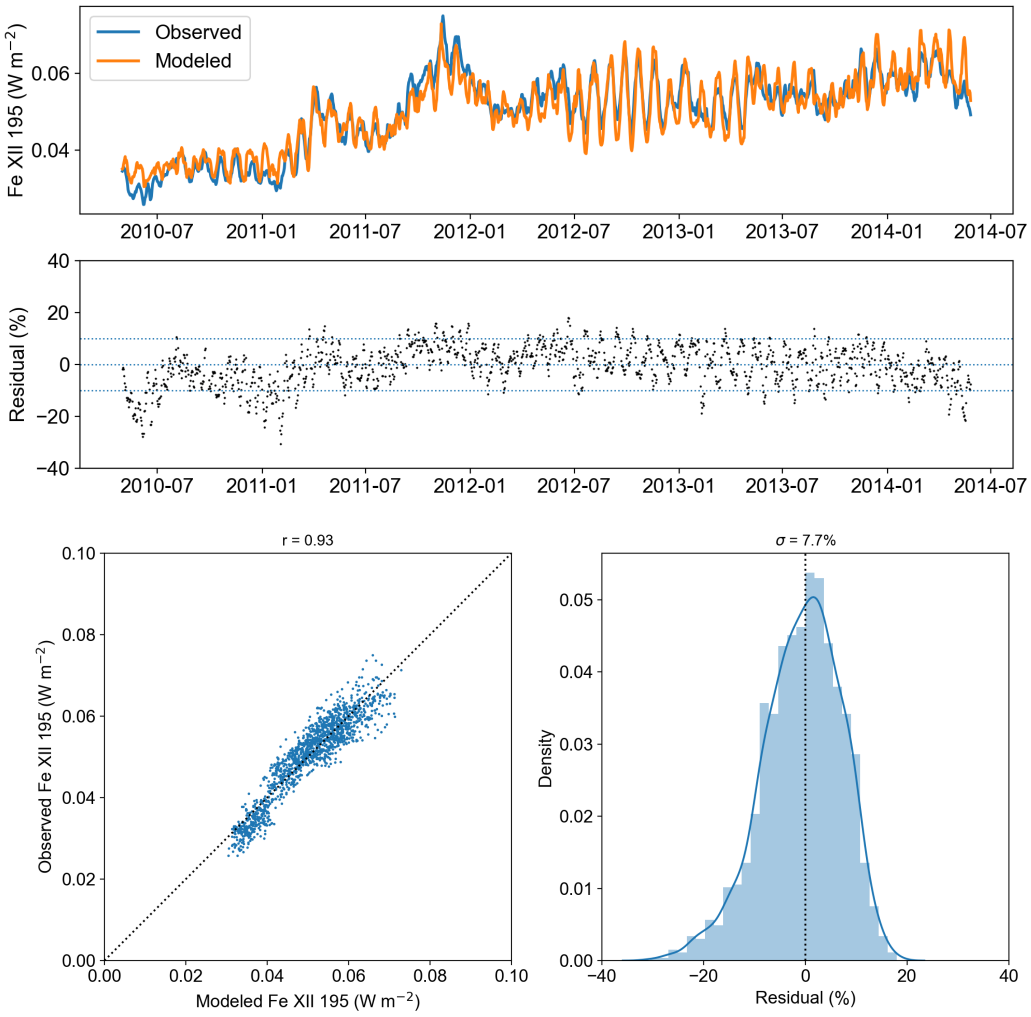

Figure 9. Results from a multiple linear regression of the magnetic flux proxy to the Fe XII 195 Å irradiance observed with EVE. The format is identical to Figure 5.

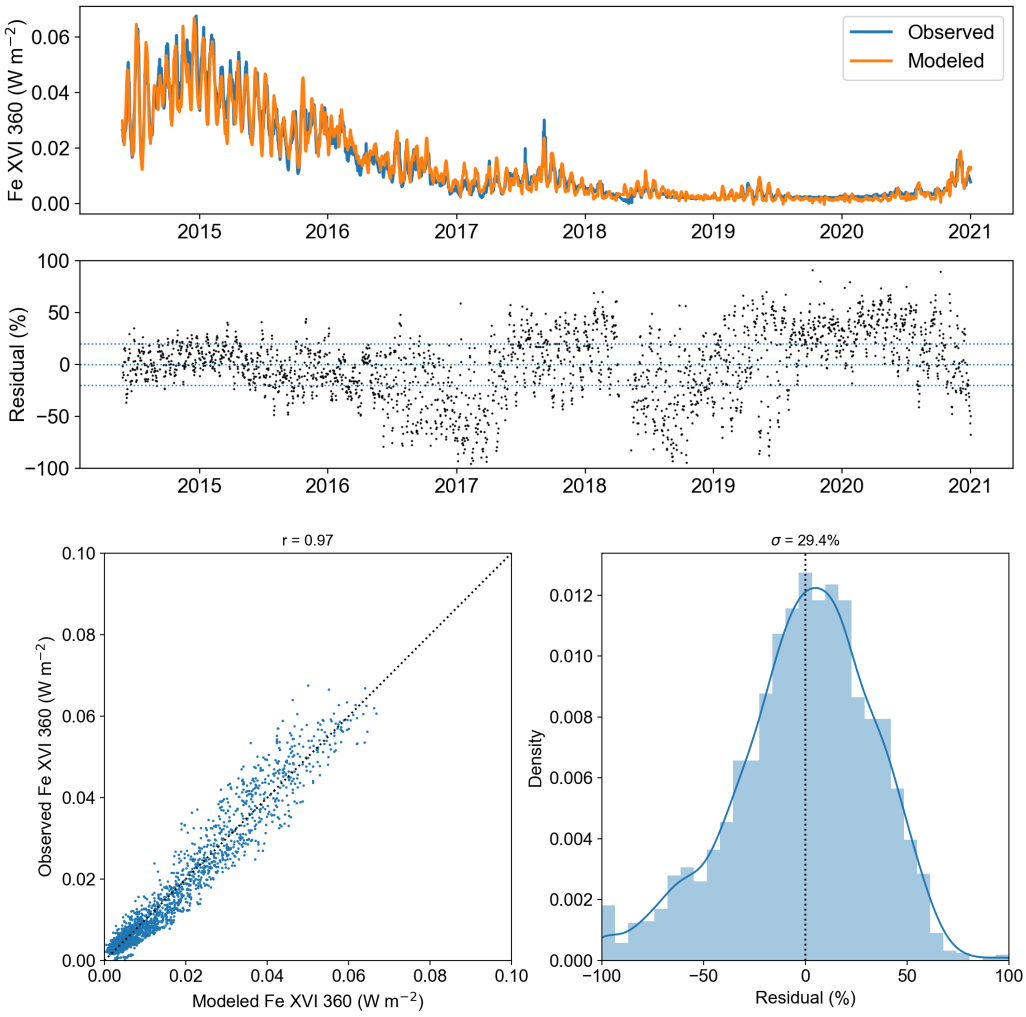

Figure 10. Results from a multiple linear regression of the magnetic flux proxy to the Fe XVI 360 Å irradiance observed with EVE.

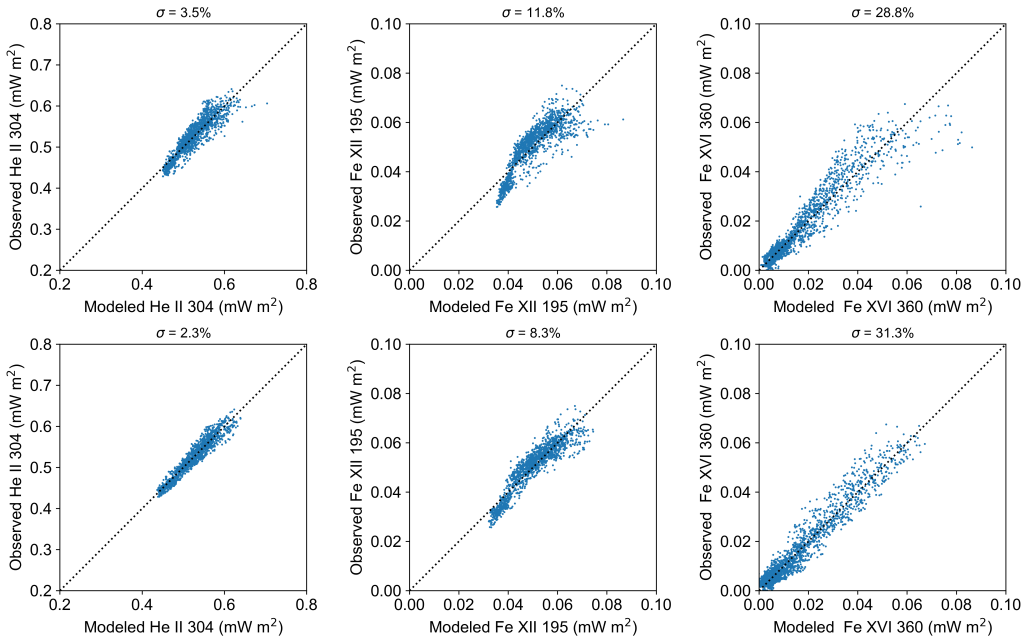

Figure 11. Scatter plots of modeled and observed EVE irradiances using the F10 and Mg core-to-wing ratio as proxies for solar activity.

4 Summary and Discussion

We have presented a new proxy for solar activity that can be used in the specification and forecasting of the solar irradiance. We have shown that this proxy can be used to accurately model other proxies for solar activity and irradiance time series formed at different layers in the solar atmosphere.

The secular trends seen in the residuals between the data and the model fits are unexpected. These trends are most clearly seen in the analysis of the Mg core-to-wing ratio data (Figure 6) and are largely absent in the fits to the EVE irradiances. To investigate the possible origins of these trends we compared the flux time series derived from the AFT images with those from the HMI observations. For the largest flux densities, above about 80 G, these time series are very similar. At smaller flux densities, however, these time series show non-trivial differences. Unfortunately, the origin of these differences is unclear. It seems that the AFT simulation modifies these weak fluxes in a way that is inconsistent with the observations. Since the assimilation of the data into the AFT model is weighted towards disk center, it is possible for these inconsistencies to persist. Of course, weak fluxes near the limb are the most difficult to measure, making it difficult to identify the origin of these differences. Ultimately, the weakest fluxes have the smallest effect on the irradiance time series and the residuals are acceptably small.

This magnetic proxy has several advantages over previous proxies. The use of spatially resolved magnetograms allows for multiple components to be defined that can reproduce emission formed at many different temperatures. While the AFT model used for this work made use of space-based magnetogram measurements, magnetograms can also be observed from the ground. The use of ground-based magnetograms should make it much easier to obtain consistent measurements over long periods of time, although this remains to be demonstrated, as long-term financial support needs to be provided for a distribution of ground based observatories. The Global Oscillation

Network Group (GONG) is an example of such a network, and a next generation GONG would provide additional important capabilities (Hill et al., 2019). Finally, the evolution of surface magnetic flux is well described by models such as AFT, which provides a physics-based framework for forecasting solar activity.

This work suggests several future research directions. For example, spatially resolved magnetogram measurements from the Mount Wilson Observatory (MWO) extend back to the early 1970's (Pevtsov et al., 2021) and our histogram analysis could be applied to these data to create a much longer magnetic proxy time series. Additionally, the skill of flux transport models in forecasting solar activity needs to be compared with simpler, statistical methods (e.g., Warren et al. (2017)). It seems likely that flux transport models will be limited by a lack of knowledge of both past far-side and future near-side flux emergence. The use of helioseismology or images from STEREO could provide a means for addressing this problem and improving flux transport simulations.

5 Data Availability Statement

We have made all of the projected magnetograms derived from the AFT flux transport simulation publicly available as standard FITS files on Zenodo (10.5281/zenodo.5094741). The total volume of data is about 11 GB. The projected magnetograms are derived from a much larger set of AFT Carrington maps of the surface magnetic field, which are not included.

All of the data products derived from the magnetograms are available on a GitHub repository

`https://github.com/USNavalResearchLaboratory/MagneticProxy`

The derived data products include the histograms of magnetic flux for each day, the PCA time series derived from the histograms, and the fit parameters for the PCA model of F10, Mg core-to-wing, the Nobeyama Radio Observatory time series, and the EVE irradiance time series. Additionally, routines for reading these derived data products are also available in the repository. The routines are written in Python and can be run with a recent distribution of Anaconda.

The F10.7 radio flux data were downloaded from

`ftp://ftp.seismo.nrcan.gc.ca/spaceweather/solar_flux/daily_flux_values/fluxtable.txt`

The Mg core-to-wing Ratio data were downloaded from

`http://www.iup.uni-bremen.de/gome/solar/MgII_composite.dat`

The Nobeyama Radio Polarimeter data were downloaded from

`https://solar.nro.nao.ac.jp/norp/data/daily/`

The EVE/SDO data were downloaded from

`https://lasp.colorado.edu/lisird/data/sdo_eve_lines_l3/`

All of these data were converted into csv files, which are included in the repository.

Acknowledgments

This work was supported by NASA's Solar Irradiance Science Team (SIST) and Living with a Star (LWS) programs as well as by the Office of Naval Research.

References

Dudok de Wit, T., Bruinsma, S., & Shibasaki, K. (2014, February). Synoptic radio observations as proxies for upper atmosphere modelling. *J. Space Weather and Space Clim.*, *4*, A06. doi: 10.1051/swsc/2014003

Gurman, J. B., Withbroe, G. L., & Harvey, J. W. (1974, January). A Comparison of EUV Spectroheliograms and Photospheric Magnetograms. *Sol. Phys.*, *34*(1), 105-111. doi: 10.1007/BF00149602

Hathaway, D. H., Williams, P. E., Dela Rosa, K., & Cuntz, M. (2010, December). The Advection of Supergranules by the Sun's Axisymmetric Flows. *ApJ*, *725*(1), 1082-1090. doi: 10.1088/0004-637X/725/1/1082

Heath, D. F., & Schlesinger, B. M. (1986, July). The Mg 280-nm doublet as a monitor of changes in solar ultraviolet irradiance. *J. Geophys. Res.*, *91*(D8), 8672-8682. doi: 10.1029/JD091iD08p08672

Henney, C. J., Hock, R. A., Schooley, A. K., Toussaint, W. A., White, S. M., & Arge, C. N. (2015, March). Forecasting solar extreme and far ultraviolet irradiance. *Space Weather*, *13*(3), 141-153. doi: 10.1002/2014SW001118

Henney, C. J., Toussaint, W. A., White, S. M., & Arge, C. N. (2012, February). Forecasting $F_{10.7}$ with solar magnetic flux transport modeling. *Space Weather*, *10*, S02011. doi: 10.1029/2011SW000748

Hill, F., Hammel, H., Martinez-Pillet, V., de Wijn, A., Gosain, S., Burkepile, J., ... Suematsu, Y. (2019, September). ngGONG: The Next Generation GONG - A New Solar Synoptic Observational Network. In *Bulletin of the american astronomical society* (Vol. 51, p. 74).

Lean, J. L., Picone, J. M., & Emmert, J. T. (2009, July). Quantitative forecasting of near-term solar activity and upper atmospheric density. *Journal of Geophysical Research (Space Physics)*, *114*(A7), A07301. doi: 10.1029/2009JA014285

Liu, Y., Hoeksema, J. T., Scherrer, P. H., Schou, J., Couvidat, S., Bush, R. I., ... Zhao, X. (2012, July). Comparison of Line-of-Sight Magnetograms Taken by the Solar Dynamics Observatory/Helioseismic and Magnetic Imager and Solar and Heliospheric Observatory/Michelson Doppler Imager. *Sol. Phys.*, *279*(1), 295-316. doi: 10.1007/s11207-012-9976-x

Pedregosa, F., Varoquaux, G., Gramfort, A., Michel, V., Thirion, B., Grisel, O., ... Duchesnay, E. (2011). Scikit-learn: Machine learning in Python. *Journal of Machine Learning Research*, *12*, 2825–2830.

Pevtsov, A. A., Bertello, L., Nagovitsyn, Y. A., Tlatov, A. G., & Pipin, V. V. (2021, January). Long-term studies of photospheric magnetic fields on the Sun. *Journal of Space Weather and Space Climate*, *11*, 4. doi: 10.1051/swsc/2020069

Scherrer, P. H., Bogart, R. S., Bush, R. I., Hoeksema, J. T., Kosovichev, A. G., Schou, J., ... MDI Engineering Team (1995, December). The Solar Oscillations Investigation - Michelson Doppler Imager. *Sol. Phys.*, *162*(1-2), 129-188. doi: 10.1007/BF00733429

Scherrer, P. H., Schou, J., Bush, R. I., Kosovichev, A. G., Bogart, R. S., Hoeksema, J. T., ... Tomczyk, S. (2012, Jan). The Helioseismic and Magnetic Imager (HMI) Investigation for the Solar Dynamics Observatory (SDO). *Sol. Phys.*, *275*, 207-227. doi: 10.1007/s11207-011-9834-2

Seabold, S., & Perktold, J. (2010). statsmodels: Econometric and statistical modeling with python. In *9th python in science conference.*

Tanaka, H., Castelli, J. P., Covington, A. E., Krüger, A., Landecker, T. L., & Tlamicha, A. (1973, March). Absolute Calibration of Solar Radio Flux Density in the Microwave Region. *Sol. Phys.*, *29*(1), 243-262. doi: 10.1007/BF00153452

Tapping, K. F. (2013, July). The 10.7 cm solar radio flux ($F_{10.7}$). *Space Weather*, *11*(7), 394-406. doi: 10.1002/swe.20064

Tiwari, S. K., Thalmann, J. K., Panesar, N. K., Moore, R. L., & Winebarger, A. R. (2017, July). New Evidence that Magnetoconvection Drives Solar-Stellar

Coronal Heating. *ApJ*, *843*(2), L20. doi: 10.3847/2041-8213/aa794c

Upton, L. A., & Hathaway, D. H. (2014a, September). Effects of Meridional Flow Variations on Solar Cycles 23 and 24. *ApJ*, *792*(2), 142. doi: 10.1088/0004-637X/792/2/142

Upton, L. A., & Hathaway, D. H. (2014b, January). Predicting the Sun's Polar Magnetic Fields with a Surface Flux Transport Model. *ApJ*, *780*(1), 5. doi: 10.1088/0004-637X/780/1/5

Upton, L. A., & Hathaway, D. H. (2018, August). An Updated Solar Cycle 25 Prediction With AFT: The Modern Minimum. *Geophys. Res. Lett.*, *45*(16), 8091-8095. doi: 10.1029/2018GL078387

Warren, H. P., Emmert, J. T., & Crump, N. A. (2017, August). Linear forecasting of the $F_{10.7}$ proxy for solar activity. *Space Weather*, *15*(8), 1039-1051. doi: 10.1002/2017SW001637

Woods, T. N., Eparvier, F. G., Hock, R., Jones, A. R., Woodraska, D., Judge, D., ... Viereck, R. (2012, Jan). Extreme Ultraviolet Variability Experiment (EVE) on the Solar Dynamics Observatory (SDO): Overview of Science Objectives, Instrument Design, Data Products, and Model Developments. *Sol. Phys.*, *275*(1-2), 115-143. doi: 10.1007/s11207-009-9487-6

Yeo, K. L., Feller, A., Solanki, S. K., Couvidat, S., Danilovic, S., & Krivova, N. A. (2014, January). Point spread function of SDO/HMI and the effects of stray light correction on the apparent properties of solar surface phenomena. *A&A*, *561*, A22. doi: 10.1051/0004-6361/201322502